Acta Materialia 187 (2020) 146–152

Contents lists available at ScienceDirect

Acta Materialia

journal homepage: www.elsevier.com/locate/actamat

Full length article

Nanopore-induced dielectric and piezoelectric enhancement in $PbTiO_3$ nanowires

Meng-Jun Zhou[a,b], Tiannan Yang[b,*], Jian-Jun Wang[b], Zhaohui Ren[c], Long-Qing Chen[b,*], Ce-Wen Nan[a,*]

[a] School of Materials Science and Engineering, State Key Lab of New Ceramics and Fine Processing, Tsinghua University, Beijing 100084, China
[b] Department of Materials Science and Engineering, The Pennsylvania State University, University Park, Pennsylvania 16802, United States
[c] State Key Laboratory of Silicon Materials, School of Materials Science and Engineering, Cyrus Tang Center for Sensor Materials and Application, Zhejiang University, 310027 Hangzhou, China

ARTICLE INFO

Article History:
Received 13 November 2019
Revised 8 January 2020
Accepted 10 January 2020
Available online 14 January 2020

Keywords:
Ferroelectric materials
Nanopore
Nanowire
Phase-field simulation

ABSTRACT

Porous tetragonal $PbTiO_3$ nanowires, synthesized through an intermediate pre-perovskite structure, exhibit distinct behaviors from those of the corresponding bulk $PbTiO_3$. Here we investigate the role of nanopores in the ferroelectric, dielectric, and piezoelectric properties of ferroelectric $PbTiO_3$ nanowires employing phase-field simulations. It is found that the presence of pores gives rise to large enhancements in both dielectric constant and piezoelectric coefficient by ~50% and 30%, respectively, compared with those of the bulk $PbTiO_3$. It is shown that the smaller the pore size is, the higher the dielectric and piezoelectric responses of the nanowire are. A charge compensation mechanism is proposed to explain the experimentally measured change of oxygen ions concentration at the pore surfaces. The findings provide in-depth insights into modulation of material properties through nanopores.

1. Introduction

Ferroelectric materials find a variety of applications such as ferroelectric random access memories (FRAMs), sensors, actuators, and microelectromechanical systems (MEMS) [1–5]. The demand for device minimization has led to extensive experimental and theoretical efforts on the low-dimension ferroelectrics, such as thin films [5–9], nanowires [10–20], nanotubes [3,21,22], etc., have been carried out recently.

Lead titanate ($PbTiO_3$), a prototypical ferroelectric material of the ABO_3 perovskites [23–28], is a model system for understanding the ferroelectric properties and related phenomena at the nanoscale [29,30]. There are two known structures for $PbTiO_3$ (PTO), its room-temperature tetragonal phase (TP) and high-temperature cubic phase (CP) [31]. Recently, a new phase, named as pre-perovskite phase (PP) with a significantly larger molar volume than either TP and CP phases, was discovered in PTO nanowires fabricated through a hydrothermal method [11,13–20,32–34]. Annealed at temperatures higher than 350°C, the PP phase was found to transform into the TP phase, resulting in the appearance of nanopores in the nanowires due to the higher density of TP phase than the PP phase [13,18]. A number of interesting behaviors were observed for the TP phase, including near-zero thermal expansion [13], enhanced piezoelectric properties [18], and inhomogeneous distribution of oxygen ions [13]. However, the underlying mechanisms for these phenomena are not well understood [13].

In this work, we employed the phase-field model of ferroelectrics [3,24] to study the effects of nanopores on phase transition and ferroelectric properties in PTO nanowires taking into account of charge compensation and surface stress. In particular, we study the influence of nanopores on the dielectric constant ε_{r33} and piezoelectric coefficient d_{33} in the PTO nanowire and compare them with those in bulk PTO. We also determine the temperature dependence of lattice parameters and inhomogeneous distributions of polarization and depolarization field and discuss their effect on oxygen vacancy distribution.

2. Phase-field model

In the phase-field model of ferroelectrics, the temporal evolution of the polarization **P** can be obtained by solving the time-dependent Ginzburg–Landau equation [3,19]:

$$\frac{\partial \mathbf{P}}{\partial t} = -L\frac{\delta F}{\delta \mathbf{P}}, \tag{1}$$

with L relating to the domain wall mobility. Eq. (1) is numerically solved with the boundary condition of $\partial\mathbf{P}/\partial n = 0$ (n being the surface normal) [35,36] on all outside surfaces of a nanowire.

* Corresponding authors.
E-mail addresses: tuy123@psu.edu, tiannan.yang@gmail.com (T. Yang), lqc3@psu.edu (L.-Q. Chen), cwnan@mail.tsinghua.edu.cn (C.-W. Nan).

https://doi.org/10.1016/j.actamat.2020.01.023
1359-6454/

The total free energy F in Eq. (1) includes bulk energy, gradient energy, elastic energy, and electrostatic energy [24]:

$$F = \int_V f dx^3 = \int_V \left(f_{\text{bulk}} + f_{\text{gradient}} + f_{\text{elastic}} + f_{\text{electrostatic}}\right) dx^3, \tag{2}$$

where $\mathbf{x} = (x_1, x_2, x_3)$ is the position vector. The bulk free energy density f_{bulk} for porous PTO nanowires is given by

$$f_{\text{bulk}} = \rho f_{\text{bulk}}^{\text{PTO}} + (1-\rho) f_{\text{bulk}}^{\text{void}}, \tag{3}$$

where $\rho(\mathbf{x})$ represents an order parameter for describing the PTO bulk ($\rho = 1$) and the pores ($\rho = 0$). A diffuse interface between each pore and the PTO bulk is adopted following $\rho\left(\mathbf{x}\right) = \left(1 + \tanh\left(\beta\left(d(\mathbf{x}) - R\right)\right)\right)/2$, where $d(\mathbf{x})$ is the distance between the position $\mathbf{x}$ and the center of its nearest pore, R is the pore radius, and $\beta = 2/3$ nm^{-1} corresponding to an interface width of 3 nm. For the PTO bulk region, a 6$^{\text{th}}$-order polynomial of the polarization [5] is used to describe the bulk energy density,

$$\begin{aligned} f_{\text{bulk}}^{\text{PTO}} = \; & \alpha_1(P_1^2 + P_2^2 + P_3^2) + \alpha_{11}(P_1^4 + P_2^4 + P_3^4) + \alpha_{12}(P_1^2P_2^2 + P_2^2P_3^2 + P_1^2P_3^2) \\ & + \alpha_{111}(P_1^6 + P_2^6 + P_3^6) + \alpha_{112}\left[(P_1^2 + P_2^2)P_3^2 + (P_1^2 + P_3^2)P_2^2 + (P_2^2 + P_3^2)P_1^2)\right] \\ & + \alpha_{123}P_1^2P_2^2P_3^2 \end{aligned} \tag{4}$$

where $\alpha_1(T) = 3.8 \times 10^5\ (T - 752.15)$ C^{-2}m^{2}N, $\alpha_{11} = -7.3 \times 10^7$ C^{-4}m^{6}N, $\alpha_{12} = 7.5 \times 10^8$ C^{-4}m^{6}N, $\alpha_{111} = 2.6 \times 10^8$ C^{-6}m^{10}N, $\alpha_{112} = 6.1 \times 10^8$ C^{-6}m^{10}N, and $\alpha_{123} = -3.7 \times 10^9$ C^{-6}m^{10}N [37,38], and temperature T in K. For pores, we use the following expression to describe the bulk energy density,

$$f_{\text{bulk}}^{\text{void}} = \alpha_1^p(P_1^2 + P_2^2 + P_3^2), \tag{5}$$

where $\alpha_1^p = 1.4 \times 10^9$ C^{-2}m^{2}N is assumed.

The gradient energy density is given by Wang et al. [39]

$$\begin{aligned} f_{\text{gradient}} = \; & \frac{1}{2}\gamma_{11}\left(\left(\frac{\partial P_1}{\partial x_1}\right)^2 + \left(\frac{\partial P_2}{\partial x_2}\right)^2 + \left(\frac{\partial P_3}{\partial x_3}\right)^2\right) \\ & + \frac{1}{2}\gamma_{44}\left(\left(\frac{\partial P_1}{\partial x_2} + \frac{\partial P_2}{\partial x_1}\right)^2 + \left(\frac{\partial P_1}{\partial x_3} + \frac{\partial P_3}{\partial x_1}\right)^2 + \left(\frac{\partial P_2}{\partial x_3} + \frac{\partial P_3}{\partial x_2}\right)^2\right) \\ & + \frac{1}{2}\gamma_{44m}\left(\left(\frac{\partial P_1}{\partial x_2} - \frac{\partial P_2}{\partial x_1}\right)^2 + \left(\frac{\partial P_1}{\partial x_3} - \frac{\partial P_3}{\partial x_1}\right)^2 + \left(\frac{\partial P_2}{\partial x_3} - \frac{\partial P_3}{\partial x_2}\right)^2\right), \end{aligned} \tag{6}$$

where γ_{ij} are the gradient energy coefficients taken as $\gamma_{11} = 3.45 \times 10^{-10}$ C^{-2}m^{4}N, $\gamma_{44} = \gamma_{44m} = {}^1\!/_2\,\gamma_{11}$ [40].

The elastic free energy density [37,39] can be calculated using

$$f_{\text{elastic}} = \frac{1}{2}c_{ijkl}(\boldsymbol{\varepsilon}_{ij} - \boldsymbol{\varepsilon}_{ij}^0)(\boldsymbol{\varepsilon}_{kl} - \boldsymbol{\varepsilon}_{kl}^0). \tag{7}$$

where the Einstein summation convention over repeated indices i,j,k,l = 1,2,3 is adopted. $\mathbf{c}$ is the elastic stiffness tensor. To distinguish the PTO phase and the pore regions, the elastic stiffness tensor takes the form of $\mathbf{c} = \rho\mathbf{c}^{\text{PTO}}$, where $\mathbf{c}^{\text{PTO}}$ represents the elastic stiffness tensor of the PTO bulk region in cubic reference phase with $c_{11} = 1.746 \times 10^{11}$ Pa, $c_{12} = 0.7937 \times 10^{11}$ Pa, and $c_{44} = 1.111 \times 10^{11}$ Pa. The total strain $\boldsymbol{\varepsilon}$ is obtained by solving the mechanical equilbrium equation [35,36]

$$\frac{\partial \boldsymbol{\sigma}_{ij}}{\partial x_j} = 0, \tag{8}$$

with the stress given by $\boldsymbol{\sigma}_{ij} = c_{ijkl}(\boldsymbol{\varepsilon}_{kl} - \boldsymbol{\varepsilon}_{kl}^0)$. The eigenstrain $\boldsymbol{\varepsilon}^0$ arising from the polarization order and the surface stress is given by

$$\boldsymbol{\varepsilon}_{ij}^0 = Q_{ijkl}P_kP_l - s_{ijkl}\boldsymbol{\sigma}_{kl}^S, \tag{9}$$

where $\mathbf{Q}$ is the electrostrictive coefficient of PTO with $Q_{11} = 0.084$ m^{4}C^{-2}, $Q_{12} = -0.026$ m^{4}C^{-2}, and $Q_{44} = 0.0675$ m^{4}C^{-2}, as determined from the experimentally measured lattice parameters [34]. $\mathbf{s} = \mathbf{c}^{-1}$is the compliance tensor, and $\boldsymbol{\sigma}^S$ is the surface stress tensor at the pore surfaces. Following [41,42],$\boldsymbol{\sigma}^S$ is a function of the spatial gradient of ρ,

$$\boldsymbol{\sigma}^S = \kappa\begin{pmatrix} \left(\frac{\partial\rho}{\partial x_2}\right)^2 + \left(\frac{\partial\rho}{\partial x_3}\right)^2 & -\frac{\partial\rho}{\partial x_1}\frac{\partial\rho}{\partial x_2} & -\frac{\partial\rho}{\partial x_1}\frac{\partial\rho}{\partial x_3} \\ -\frac{\partial\rho}{\partial x_1}\frac{\partial\rho}{\partial x_2} & \left(\frac{\partial\rho}{\partial x_1}\right)^2 + \left(\frac{\partial\rho}{\partial x_3}\right)^2 & -\frac{\partial\rho}{\partial x_2}\frac{\partial\rho}{\partial x_3} \\ -\frac{\partial\rho}{\partial x_1}\frac{\partial\rho}{\partial x_3} & -\frac{\partial\rho}{\partial x_2}\frac{\partial\rho}{\partial x_3} & \left(\frac{\partial\rho}{\partial x_1}\right)^2 + \left(\frac{\partial\rho}{\partial x_2}\right)^2 \end{pmatrix}. \tag{10}$$

Here $\kappa = 3.8 \times 10^{-8}$ J/m is the gradient energy coefficient of ρ. In addition to the surface stress at the pore surfaces, the surface stress on the external surfaces of the PTO nanowire is also considered by applying a stress boundary condition $\boldsymbol{\sigma}_n = -\mu/R_W$ on the side surface of a cylindrical nanowire. μ is the scalar surface stress parameter with a typcial value of 5–30 J/m^2 [43,44], taken as $\mu = 9$ J/m^2 in the present work. R_W is the radius of the nanowire taken as $R_W = 50$ nm following a medium value within the experimental range of 10–250 nm [13,17]. The normal surface stress component $\boldsymbol{\sigma}_n$ is perpendicular to the outside surface of the nanowire [39]. The effect of surface stress on the polarization and stress distribution is discussed in Supporting Information.

The electrostatic energy density is calculated by

$$f_{\text{electrostatic}} = -P_iE_i - \frac{1}{2}\boldsymbol{\varepsilon}_0\boldsymbol{\varepsilon}_{ij}^bE_iE_j. \tag{11}$$

where $\boldsymbol{\varepsilon}_0$ and $\boldsymbol{\varepsilon}^b$ are the vacuum dielectric constant and the background dielectric constant [45], respectively. The spatial distribution of the electric field $\mathbf{E}$ is obtained by solving the electrostatic equilibrium equation in the absence of free charges,

$$\nabla \cdot \mathbf{D} = 0 \tag{12}$$

where the electric displacement $\mathbf{D}$ is given by

$$\mathbf{D} = \boldsymbol{\varepsilon}_0\boldsymbol{\varepsilon}^b\mathbf{E} + \mathbf{P}. \tag{13}$$

There have been experimental reports on migration and redistribution of the oxygen ions (O^{2-}) in porous PTO nanowires, forming an inhomogeneous concentration of O^{2-} ions, which provides partial compensation to the bound charges arising from the polarization inhomogeneity in the nanowire [13]. Such effect is especially strong near the surfaces of the nanopores with a ~5% fluctuation in the molar fraction of O^{2-}. This indicates an ionic contribution to the electrostatic screening in the nanowire in addition to the electronic contribution. In the present phase-field model, by assuming that the screening effect is linearly dependent on the local electric field, such ionic contribution is implicitly treated by absorbing it into the background dielectric constant $\boldsymbol{\varepsilon}^b$. Due to the cubic symmetry of the high-temperature CP-PTO phase, the background dielectric constant tensor satisfies $\boldsymbol{\varepsilon}_{ii}^b = \boldsymbol{\varepsilon}^b$ and $\boldsymbol{\varepsilon}_{ij}^b = 0 (i \neq j)$. Here, $\boldsymbol{\varepsilon}^b$ is assumed as

$$\boldsymbol{\varepsilon}^b = 950\exp\left(-T^b/T\right), \tag{14}$$

due to an Arrhenius-type temperature dependence of the ionic defect concentration, with $T^b = 550$ K.

The local concentration distribution of the O^{2-} ions in the porous PTO nanowires can be estimated from the electric-field distribution. The total electric charge density $\rho_e^{\text{total}} = \boldsymbol{\varepsilon}_0 \nabla \cdot \mathbf{E}$ consists of two parts: 1) the bound charge $\rho_e^{\text{bound}} = -\nabla \cdot \mathbf{P}$ related to the polarization field and 2) the background charge $\rho_e^{\text{background}}$ containing both ionic and electronic contributions, identified as

$$\rho_e^{\text{background}} = \rho_e^{\text{total}} - \rho_e^{\text{bound}} = \boldsymbol{\varepsilon}_0 \nabla \cdot \mathbf{E} + \nabla \cdot \mathbf{P} = -\boldsymbol{\varepsilon}_0(\boldsymbol{\varepsilon}^b - 1) \nabla \cdot \mathbf{E}. \tag{15}$$

For a quick estimation, we attribute $\rho_e^{\text{background}}$ only to the ionic contribution and neglect the electronic contribution. The background charge density is then related to the ion concentration c_v as

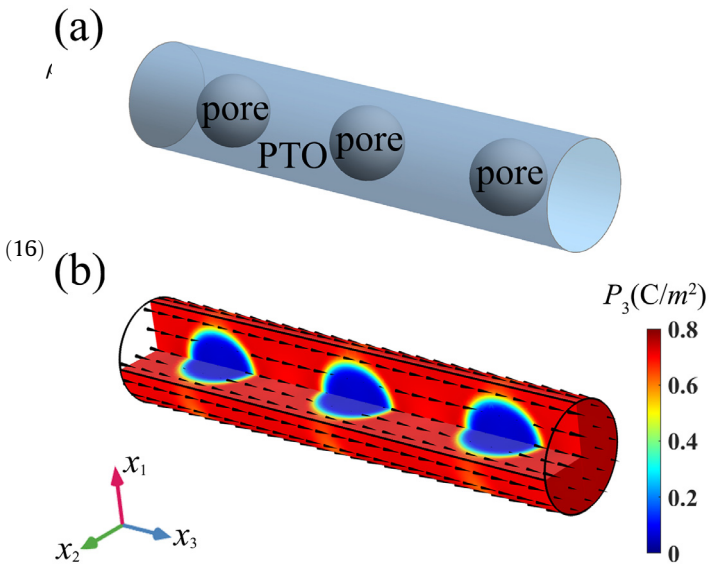

Fig. 1. (a) Schematic of the porous PTO nanowire. (b) Polarization distribution in the porous nanowires. The direction and size of the black arrows indicate the direction and magnitude of the polarization vector, and the background color represents the intensity of P_3 (see the color bar).

Due to the relatively large mass of Pb^{2+} and Ti^{4+} ions compared with the O^{2-} ion, their migration under an electric field can be ignored. Therefore, we assume a fixed concentration of Pb^{2+} and Ti^{4+} ions which is the same as that in perfect PTO crystals, i.e.,

$$c_v(Pb^{2+}) = c_v(Ti^{4+}) = \frac{1}{V_0}. \tag{17}$$

Here, $V_0 = a^2c$ is the unit cell volume (a and c being the lattice parameters of the tetragonal phase PTO [20]). Combining Eqs. (15)–(17), the concentration of O^{2-} ions is given by

$$c_v(O^{2-}) = \frac{-\varepsilon_0(\varepsilon^b - 1)\nabla \cdot \mathbf{E}}{-2e^-} + \frac{3}{V_0}, \tag{18}$$

And the molar fraction of O^{2-} ions follows

$$c(O^{2-}) = \frac{c_v(O^{2-})V_0}{5} \times 100\% \tag{19}$$

3. Results and discussions

We first model a TP-PTO nanowire containing 3 identical spherical pores with a radius of R = 6.8 nm, as illustrated in Fig. 1 (a). The radius and length of the nanowire are taken as 10 nm and 100 nm, respectively, which are smaller than experimental values due to computation load concerns. The total volume of the pores takes up 13% that of the nanowire, which is established under an assumption of a constant volume of the PTO nanowire during the PP-PTO → TP-PTO phase transition and the fact that the density of PP-PTO is 87% that of the TP-PTO [13]. A diffuse pore surface with a thickness of 3 nm is adopted. The equilibrium polarization distribution in the porous TP-PTO nanowire at T = 293 K is shown in Fig. 1(b). As seen, a ferroelectric single domain is formed with the polarization along the axis of the nanowire, which is consistent with previous experimental reports [13]. Furthermore, the magnitude of the polarization in the PTO phase is mostly uniform except for a decrease in regions near the surfaces of the pores.

The average polarization P_3 in the porous PTO nanowire at different temperatures is shown in Fig. 2(a). The simulated results on the bulk PTO are also provided for comparison. As seen, at temperatures far below the Curie temperature of the ferroelectric phase transition, the nanowire shows a slightly smaller polarization than that of the bulk PTO due to the existence of pores. For example, at T = 293 K, the average polarization of the nanowire is P_3 = 0.67 C/m^2, which is 11.8% lower than that of the bulk at P_3 = 0.76 C/m^2. The polarization difference increases with temperature (e.g., 18.7% at T = 593 K). A ferroelectric-to-paraelectric phase transition occurs upon further increasing the temperature in both systems, where the nanowire shows a decreased Curie temperature of T_C = 715 K compared to the bulk at T_C = 765 K.

Similar to the polarization, the c/a ratio of the lattice parameters of the porous PTO nanowire, as provided Fig. 2(b), shows a decrease from that of the bulk PTO. The temperature dependence of the c/a ratio from the phase-field model also shows a very good agreement with experimental measurements for both the nanowire and the bulk [13].

It is found that the ionic contribution to the charge compensation strongly affects the polarization and c/a ratio of the porous PTO nanowire. For example, if we only considered the electronic charge compensation with a temperature-independent background dielectric constant of ε^b = 145 and neglect the ionic part, both the polarization and c/a ratio would decrease much faster with increase in temperature and would deviate significantly from the experimental data (see

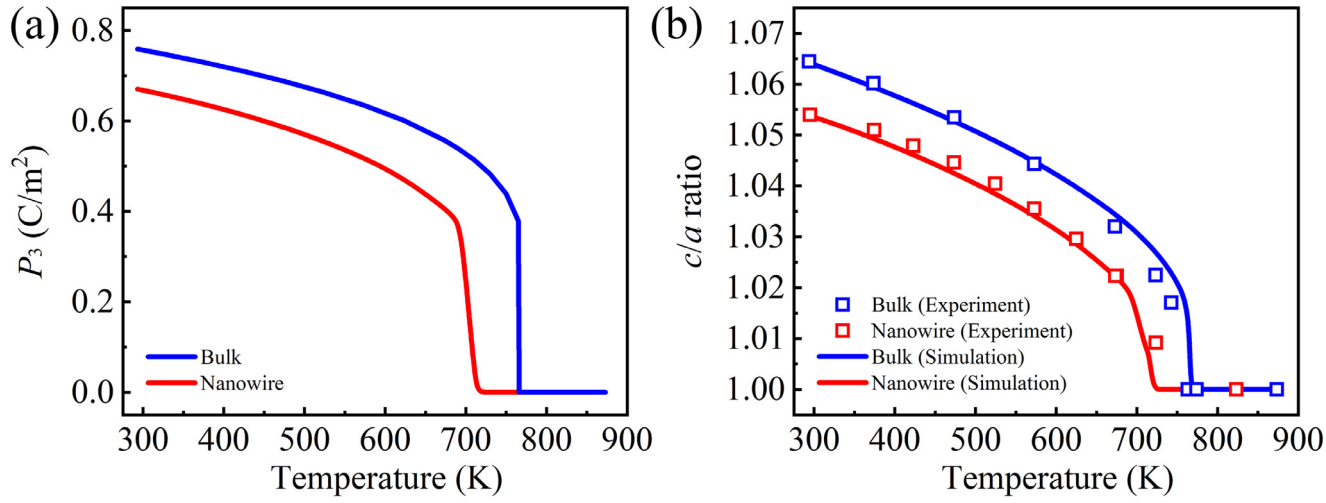

Fig. 2. (a) Average polarization P_3 and (b) c/a ratio of the porous PTO nanowire and the bulk PTO as a function of temperature. The blue and red squares are the experimental data for the bulk PTO and the porous PTO nanowire, respectively [13]. (For interpretation of the references to color in this figure legend, the reader is referred to the web version of this article.)

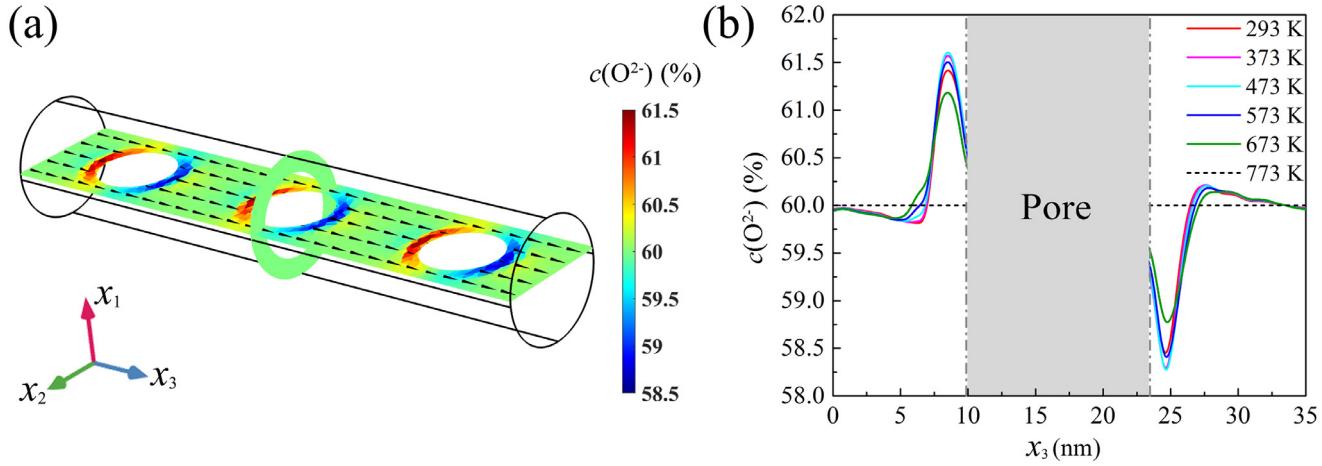

Fig. 3. (a) The distribution of molar fraction of O^{2-} ions in two perpendicular cross sections in the porous PTO nanowires at T = 293 K. (b) The molar fraction of O^{2-} ions along the central axis of the porous PTO nanowire across one pore at different temperatures.

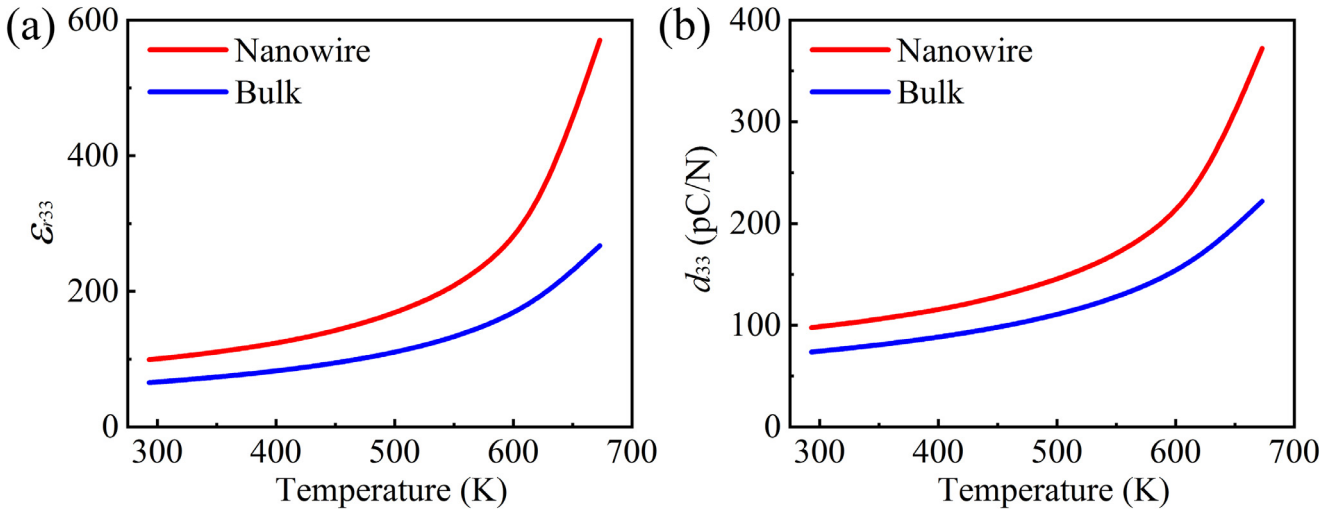

Fig. 4. (a) Effective dielectric constant ε_{r33} and (b) effective piezoelectric coefficient d_{33} of the porous PTO nanowire and the bulk PTO as a function of temperature.

Fig. S1). Hence, the ionic charge compensation is crucial to the polarization distribution and lattice parameters of the PTO nanowire.

Fig. 3 (a) shows the distribution of molar fraction of O^{2-} ions in a PTO nanowire at T = 293 K, which shows a change from $c(O^{2-})$ = 61.4% to $c(O^{2-})$ = 58.5% across a pore along the axis of the nanowire. The difference of $\Delta c(O^{2-})$ = 2.9 across the pore agrees with the experimentally measured value of 5% in previous report [13]. Such a variation in $c(O^{2-})$ provides partial compensation to the bound charges arising from polarization discontinuity around a pore surface. In the cross section perpendicular to the axis of the nanowire across each pore, $c(O^{2-})$ is mostly unchanged with $c(O^{2-})$ = 60%, the same value as a perfect PTO crystal, which is also consistent with the experimental measurement [13]. These agreements with experiments support the use of ionic charge compensation mechanisms in the phase-field model.

The distribution of $c(O^{2-})$ across each pore in a porous nanowire at higher temperatures is examined and shown in Fig. 3(b). Upon increase in temperature, the difference in $c(O^{2-})$ between the two sides of the pore along the axis of the nanowire first slightly increases till reaching a maximum value of $\Delta c(O^{2-})$ = 3.4% at T = 473 K, and then starts to decrease and eventually disappears at T = 773 K. Such a temperature dependence is mainly caused by the competition between the two mechanisms: 1) the enhanced charge compensation at low temperature ($\boldsymbol{\varepsilon}^b$ increases following Eq. (13)) resulting in an increase of $\Delta c(O^{2-})$, and 2) the decreased polarization near Curie temperature leading to a decrease of $\Delta c(O^{2-})$.

We next study the dielectric and piezoelectric properties of a porous PTO nanowire. The effective dielectric constant of the nanowire is calculated from the polarization response to an applied electric field E_3 = 0.1 MV/m following $\boldsymbol{\varepsilon}_{rij} = \Delta P_i/(\boldsymbol{\varepsilon}_0 \Delta E_j)$, and the results are shown in Fig. 4(a). The dielectric constant $\boldsymbol{\varepsilon}_{r33}$ of the porous PTO nanowire shows a notable enhancement from that of the bulk PTO within calculated temperature ranges. For example, at T = 293 K, the effective dielectric constant of the nanowire is $\boldsymbol{\varepsilon}_{r33}$ = 99, which is 52.3% higher than that of the bulk at $\boldsymbol{\varepsilon}_{r33}$ = 65. Such enhancement is stronger at higher temperatures, e.g., $\boldsymbol{\varepsilon}_{r33}$ = 570 at T = 673K, with a 113% enhancement from the bulk at $\boldsymbol{\varepsilon}_{r33}$ = 267. Other than the dielectric constant, an enhancement of the piezoelectric coefficient is also found in the PTO nanowire. Fig. 4(b) shows d_{33} following $d_{33} = \Delta\boldsymbol{\varepsilon}_{33}/\Delta E$ obtained from the strain change upon applying an applied electric field. As seen, the nanowire shows a piezoelectric coefficient d_{33} = 98 pC/N at T = 293 K, which is enhanced by 32.3% over the value 74 pC/N of a bulk crystal. The enhancement of the piezoelectric coefficient is in agreement with previous experimental measurement [18]. Similar to the dielectric constant, the enhancement in d_{33} of the nanowire also slightly increases with increasing temperature, reaching 68.3% enhancement at T = 673 K.

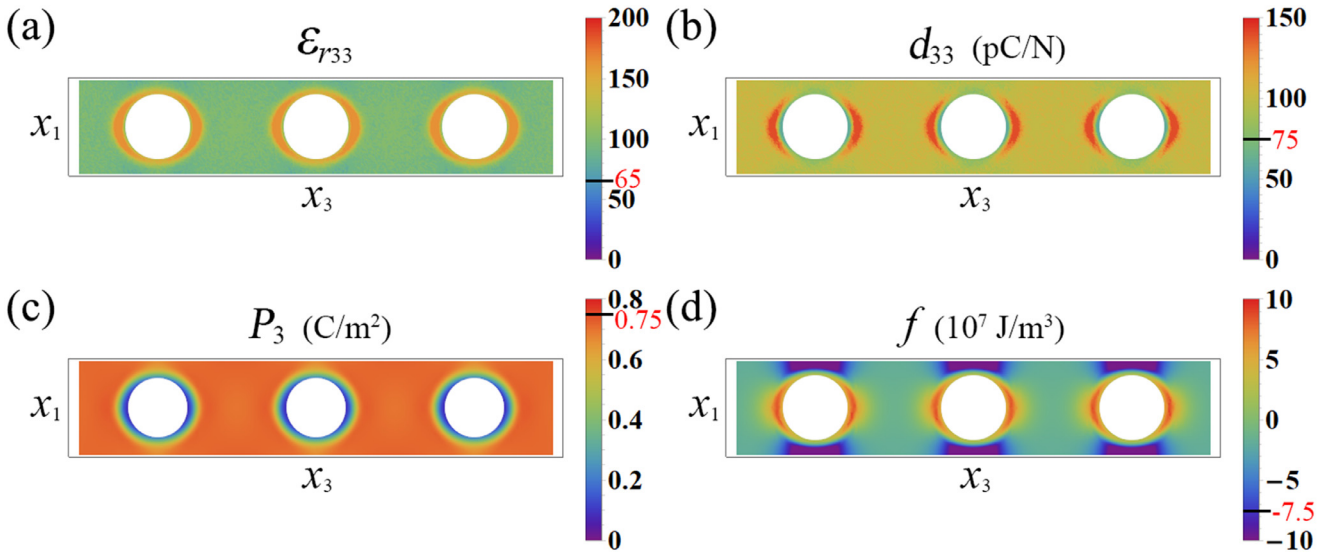

Fig. 5. Spatial distribution of (a) the dielectric constant ε_{r33}, (b) the piezoelectric coefficient d_{33}, (c) polarization P_3, and (d) energy density f at T = 293 K in the central x_1- x_3 cross section of the PTO nanowire. The black lines with red numbers at the color bars indicate the corresponding values of the bulk PTO.

To understand the dielectric and piezoelectric enhancements of the nanowire, a close examination on the spatial profiles of the dielectric and piezoelectric responses in the PTO nanowire is performed. As presented in Fig. 5(a), the dielectric responses in most regions of the nanowire show enhancements of ε_{r33} = 90−110 over the bulk value of 65. In addition, regions around the pore surface undergo an even stronger response to $\varepsilon_{r33} \geq 150$, with the highest value reaching ε_{r33} = 214. Such enhanced dielectric responses result from the locally reduced polarization stability relating to a decreased polarization [46] and an elevated free energy caused by the existence of the nanopores. For example, Fig. 5(c) and (d) show the spatial distributions of the polarization P_3 and the total free energy density f under zero field. As seen, regions around the pore surfaces show a much-reduced local polarization with an elevated free energy in comparison to the bulk PTO. As a result, these regions exhibit the strongest polarization responses upon applying an external field. The rest of the PTO phase show a relatively smaller difference in both the polarization and free energy from those of the bulk. Similar phenomenon is observed in the piezoelectric response, with the strongest response up to d_{33} = 180 pC/N around the surfaces of the pores, as shown in Fig. 5(b), demonstrating the direct connection between reduced local polarization stability and the enhanced properties.

We further investigate the effect of the pore size on the structure and properties of the porous PTO nanowires. Fig. 6(a) illustrates the structures of four PTO nanowires with different pore radii R used in the present work. The total volume fraction of the nanopores is fixed at 13%. The c/a ratio of the four different PTO nanowires is shown in Fig. 6(b). It can be observed that the c/a ratio decreases with increasing temperature for all PTO nanowires. In addition, a notable decrease in the c/a ratio with decreasing pore radius is observed at all temperatures. This is understood as the effect of the increased total surface area of the pores on the polarization reduction, since the total number of pores increases with decreasing pore size and a fixed a total volume of the pores. It is also worth noting that previous experimental reports indicated an increasing c/a ratio of PTO nanowires that are prepared with increasing annealing time from 5 min to 180 min [13]. Since the pores in the nanowire merge during the annealing process, a longer annealing time can give rise to fewer pores with a larger pore size, bringing possible connections to the c/a ratio of the nanowire. As shown in Fig. 6(b), the experimentally measured c/a ratios of the porous PTO nanowires after annealing for 5 min, 30 min, and 180 min agree well with the simulated values of PTO nanowires with a pore radius of R = 4.1 nm, 5.2 nm, and 6.8 nm, respectively. Therefore, the observed annealing time effect on the c/a ratio can be attributed the result of the effect of the pore size.

Fig. 6(c) shows the effective dielectric constant ε_{r33} of the porous PTO nanowires with different pore sizes. It is found that ε_{r33} increases with temperature for all four PTO nanowires. In addition, within the whole temperature range of T = 293−673 K, ε_{r33} also undergoes a rapid increase with a decreasing pore radius. For example, ε_{r33} increases from 99 to 160 with the pore radius decreasing from 6.8 nm to 3.1 nm at T = 293 K. As has been established earlier, the dielectric response is greatly enhanced around the pore surfaces of the PTO nanowire. Hence, such a pore size dependence of the dielectric constant is also a natural result of a larger total surface area of pores within PTO nanowires with a smaller pore size and a fixed total volume fraction of pores.

The effective piezoelectric coefficient d_{33} of the different PTO nanowires is shown in Fig. 6(d). Similar to ε_{r33}, the PTO nanowires show higher d_{33} with smaller pore radii resulted from the larger total pore surface area. However, in the PTO nanowire with a pore radius of R = 3.1 nm, d_{33} undergoes an abnormal decrease with temperature at $T >$ 623 K, which is absent in nanowires with other radii. In fact, the PTO nanowire with R = 3.1 nm shows a lower d_{33} than the one with R = 4.1 nm at temperatures $T >$ 650 K. This is understood by the concurrent action of the temperature dependence of the polarization and that of its response to an external field. Taking the relation $d_{mij} = 2Q_{ijkl}P_k\varepsilon_{lm}$ [47] of the piezoelectric coefficient of a homogeneous system, as the electrostrictive coefficient $\mathbf{Q}$ is mostly independent of the temperature, $d_{33}(T)$ is determined by the product of the dielectric constant ε_{r33} and the polarization P_3. In most cases, the effective dielectric constant ε_{r33} of the nanowire shows a stronger temperature dependence than that of the average polarization P_3, giving rise to an increasing $d_{33}(T)$ due to the increasing $\varepsilon_{r33}(T)$. The exception of the PTO nanowire with R = 3.1 nm at $T >$ 623 K is caused by the stronger polarization dependence at temperatures near the Curie temperature, where the decrease in $P_3(T)$ becomes dominant, resulting in the decreasing $d_{33}(T)$ with increasing temperature.

4. Summary

A systematic investigation on the structure and properties of porous PTO ferroelectric nanowires is carried out using phase-field simulations. It is shown that the introduction of nanopores within the PTO nanowires significantly alters the ferroelectric, dielectric and piezoelectric properties. First, a notable enhancement of both

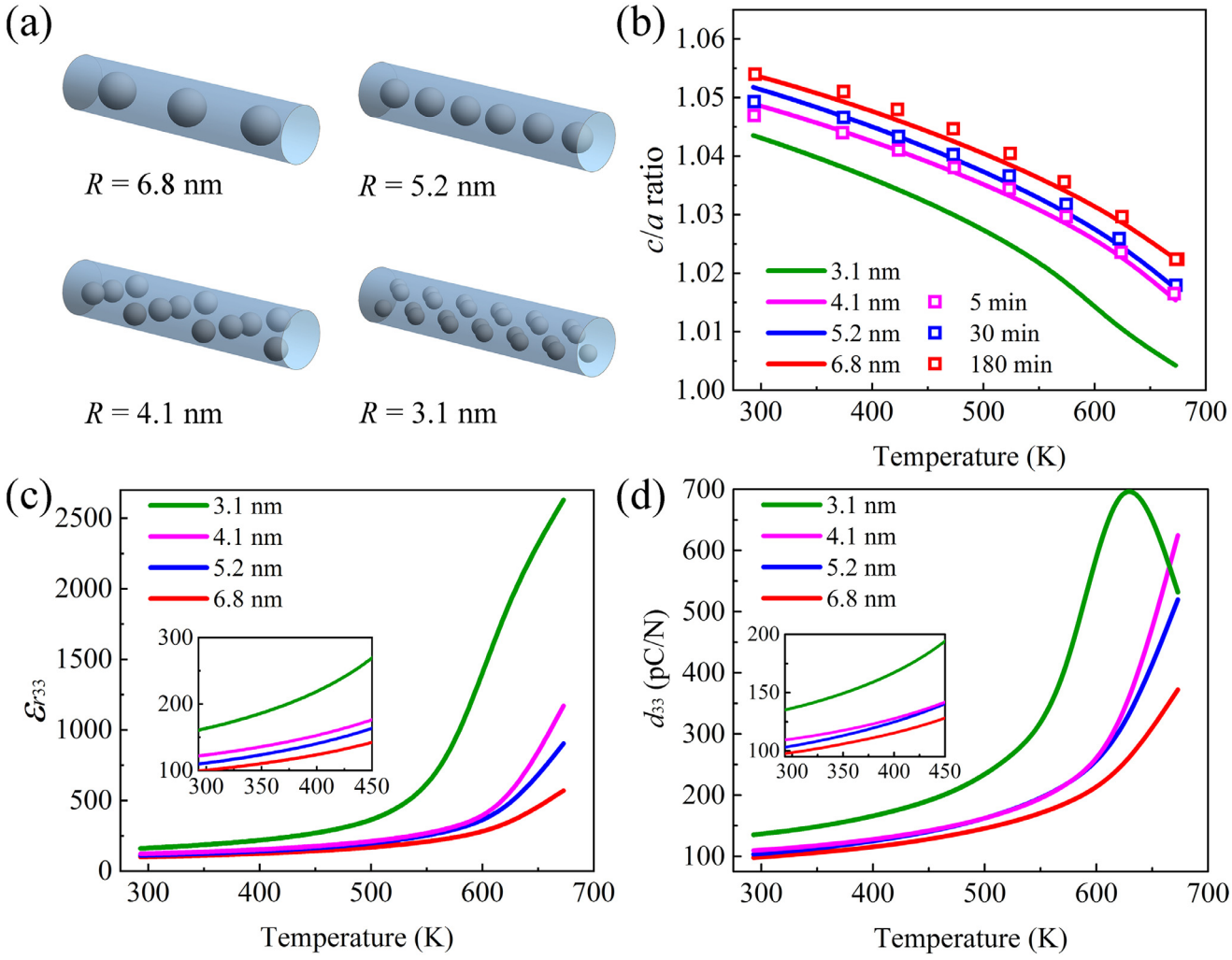

Fig. 6. (a) Schematic of 4 porous PTO nanowires with pore radii of R = 6.8 nm, 5.2 nm, 4.1 nm, and 3.1 nm, respectively. (b)–(d) (Curves) (b) c/a ratio, (c) effective dielectric constant ε_{r33}, and (d) effective piezoelectric coefficient d_{33} of the porous PTO nanowires with different pore radii as a function of temperature. 3 sets of experimentally measured c/a ratios of PTO nanowires annealed for 5 min, 30 min, and 180min, respectively [13], are plotted in (b) for comparison, as shown by the squares.

dielectric and piezoelectric performances of porous PTO nanowires is observed due to significantly enhanced polarization responses near the pore surfaces. For example, in a PTO nanowire with a pore radius of 6.8 nm at T = 293 K, the dielectric constant ε_{r33} and the piezoelectric coefficient d_{33} are enhanced by 52% and 32%, respectively, compared with those of the bulk PTO. Secondly, studies on the effect of pore size indicate that porous PTO nanowires containing smaller pores tend to have a higher dielectric constant and a higher piezoelectric coefficient. The c/a ratio of the nanowire is found to be reduced with decreasing pore size, which explains the annealing time dependence of the c/a ratio reported in previous experiments. Furthermore, a redistribution of oxygen ion concentration around the pore surfaces arising from electrostatic interactions is also demonstrated, which is consistent with previous experimental reports. This work provides an in-depth understanding of the crucial role of nanopores in tuning the properties of ferroelectric materials, which offers a new pathway for the performance optimization of ferroelectric materials.

Declaration of Competing Interest

The authors declare the following financial interests/personal relationships which may be considered as potential competing interests: Alexander K. Tagantsev, Swiss Federal Institute of Technology in Lausanne (EPFL), Switzerland.

Acknowledgments

The work at Tsinghua (M.-J. Z. and C.-W. N.) was supported by the NSF of China (Grant no. 51788104) and China Scholarship Council (no 201706210108). T. Y. and L.-Q. C. acknowledge the support from the National Science Foundation under grant number DMR-1744213. J.-J. W. and L.-Q. C. acknowledge the support from the Army Research Office under grant number W911NF-17-1-0462. The authors acknowledge support for computational resources from the Institute for CyberScience Advanced CyberInfrastructure (ICS-ACI) in the Pennsylvania State University.

Supplementary materials

Supplementary material associated with this article can be found in the online version at doi:10.1016/j.actamat.2020.01.023.

References

[1] L. Jin, F. Li, S. Zhang, Decoding the fingerprint of ferroelectric loops: comprehension of the material properties and structures, J. Am. Ceram. Soc. 97 (2014) 1–27, doi: 10.1111/jace.12773.

[2] S. Zhang, F. Li, X. Jiang, J. Kim, J. Luo, X. Geng, Advantages and challenges of relaxor-$PbTiO_3$ ferroelectric crystals for electroacoustic transducers – A review, Prog. Mater. Sci. 68 (2015) 1–66, doi: 10.1016/j.pmatsci.2014.10.002.

[3] J.-J. Wang, B. Wang, L.-Q. Chen, Understanding, predicting, and designing ferroelectric domain structures and switching guided by the phase-field method, Annu. Rev. Mater. Res. 49 (2019) 127–152, doi: 10.1146/annurev-matsci-070218-121843.
[4] J.F. Scott, C.A. Paz de Araujo, Ferroelectric memories, Science 246 (1989) 1400–1405 (80-.), doi: 10.1126/science.246.4936.1400.
[5] M.-J. Zhou, J.-J. Wang, L.-Q. Chen, C.-W. Nan, Strain, temperature, and electric-field effects on the phase transition and piezoelectric responses of $K0.5Na0.5NbO_3$ thin films, J. Appl. Phys. 123 (2018) 154106, doi: 10.1063/1.5027505.
[6] L. Zhang, J. Chen, L. Fan, O. Diéguez, J. Cao, Z. Pan, Y. Wang, J. Wang, M. Kim, S. Deng, J. Wang, H. Wang, J. Deng, R. Yu, J.F. Scott, X. Xing, Giant polarization in super-tetragonal thin films through interphase strain, Science 361 (2018) 494–497, doi: 10.1126/science.aan2433.
[7] S.W. Zhang, Z. Zhou, J. Luo, J.F. Li, Potassium-sodium-niobate-based thin films: lead free for micro-piezoelectrics, Ann. Phys. 531 (2019), doi: 10.1002/andp.201800525.
[8] J. Luo, S. Zhang, Z. Zhou, Y. Zhang, H.Y. Lee, Z. Yue, J.F. Li, Phase transition and piezoelectricity of $BaZrO_3$ -modified $(K,Na)NbO_3$ lead-free piezoelectric thin films, J. Am. Ceram. Soc. 102 (2019) 2770–2780, doi: 10.1111/jace.16172.
[9] B. Wang, H.-N. Chen, J.-J. Wang, L. Chen, Ferroelectric domain structures and temperature-misfit strain phase diagrams of $K1-xNaxNbO_3$ thin films: a phase-field study, Appl. Phys. Lett 115 (2019) 092902, doi: 10.1063/1.5116910.
[10] J.J. Wang, E.A. Eliseev, X.Q. Ma, P.P. Wu, A.N. Morozovska, L.-Q. Chen, Strain effect on phase transitions of $BaTiO_3$ nanowires, Acta Mater. 59 (2011) 7189–7198, doi: 10.1016/j.actamat.2011.08.015.
[11] R. Zhao, M. Li, Z. Ren, Y. Zhu, G. Han, Three-dimensional oriented attachment growth of single-crystal pre-perovskite $PbTiO_3$ hollowed fibers, CrystEngComm 20 (2018) 448–453, doi: 10.1039/C7CE01780D.
[12] J. Wang, K. Schenk, A. Carvalho, B. Wylie-Van Eerd, J. Trodahl, C.S. Sandu, M. Bonin, I. Gregora, Z. He, T. Yamada, H. Funakubo, P.R. Briddon, N. Setter, Structure determination and compositional modification of body-centered tetragonal PX-phase lead titanate, Chem. Mater. 23 (2011) 2529–2535, doi: 10.1021/cm1030206.
[13] Z. Ren, R. Zhao, X. Chen, M. Li, X. Li, H. Tian, Z. Zhang, G. Han, Mesopores induced zero thermal expansion in single-crystal ferroelectrics, Nat. Commun. 9 (2018) 1638, doi: 10.1038/s41467-018-04113-y.
[14] T. Yu, Z. Ren, S. Gong, S. Jiang, C. Chao, X. Li, G. Shen, G. Han, Length-controlled synthesis and the photoluminescence of pre-perovskite $PbTiO_3$ nanofibers, CrystEngComm 16 (2014) 3567–3572, doi: 10.1039/C3CE42131G.
[15] Z. Liu, Z. Ren, Z. Xiao, C. Chao, X. Wei, Y. Liu, X. Li, G. Xu, G. Shen, G. Han, Size-controlled single-crystal perovskite $PbTiO_3$ nanofibers from edge-shared TiO_6 octahedron columns, Small 8 (2012) 2959–2963, doi: 10.1002/smll.201200795.
[16] Z. Xiao, Z. Ren, Y. Xia, Z. Liu, G. Xu, X. Li, G. Shen, G. Han, Doping and phase transformation of single-crystal pre-perovskite $PbTiO_3$ fibers with TiO_6 edge-shared octahedra, CrystEngComm 14 (2012) 4520, doi: 10.1039/c2ce25104c.
[17] A. Kvasov, L.J. McGilly, J. Wang, Z. Shi, C.S. Sandu, T. Sluka, A.K. Tagantsev, N. Setter, Piezoelectric enhancement under negative pressure, Nat. Commun. 7 (2016) 12136, doi: 10.1038/ncomms12136.
[18] J. Wang, B. Wylie-Van Eerd, T. Sluka, C. Sandu, M. Cantoni, X.K. Wei, A. Kvasov, L.J. McGilly, P. Gemeiner, B. Dkhil, A. Tagantsev, J. Trodahl, N. Setter, Negative-pressure-induced enhancement in a freestanding ferroelectric, Nat. Mater. 14 (2015) 985–990, doi: 10.1038/nmat4365.
[19] Z. Ren, G. Jing, Y. Liu, J. Gao, Z. Xiao, Z. Liu, S. Yin, S. Zhou, G. Xu, X. Li, G. Shen, G. Han, Pre-perovskite nanofiber: a new direct-band gap semiconductor with green and near infrared photoluminescence, RSC Adv. 3 (2013) 5453, doi: 10.1039/c3ra23413d.
[20] Z. Ren, G. Xu, Y. Liu, X. Wei, Y. Zhu, X. Zhang, G. Lv, Y. Wang, Y. Zeng, P. Du, W. Weng, G. Shen, J.Z. Jiang, G. Han, $PbTiO_3$ nanofibers with edge-shared TiO_6 octahedra, J. Am. Chem. Soc. 132 (2010) 5572–5573, doi: 10.1021/ja1011614.
[21] J. Wang, M. Kamlah, Domain structures of ferroelectric nanotubes controlled by surface charge compensation, Appl. Phys. Lett. 93 (2008) 042906, doi: 10.1063/1.2966366.
[22] Y. Luo, I. Szafraniak, V. Nagarajan, R.B. Wehrspohn, M. Steinhart, J.H. Wendorff, N.D. Zakharov, R. Ramesh, M. Alexe, Ferroelectric lead zirconate titanate and barium titanate nanotubes, Integr. Ferroelectr. 59 (2003) 1513–1520, doi: 10.1080/10584580390260009.
[23] D. Damjanovic, Ferroelectric, dielectric and piezoelectric properties of ferroelectric thin films and ceramics, Reports Prog. Phys. 61 (1998) 1267–1324, doi: 10.1088/0034-4885/61/9/002.
[24] L.-Q. Chen, Phase-field method of phase transitions/domain structures in ferroelectric thin films: a review, J. Am. Ceram. Soc. 91 (2008) 1835–1844, doi: 10.1111/j.1551-2916.2008.02413.x.
[25] G. Shirane, S. Hoshino, On the phase transition in lead titanate, J. Phys. Soc. Jpn. 6 (1951) 265–270, doi: 10.1143/JPSJ.6.265.
[26] H. Fang, Y. Wang, S.-L. Shang, Z.-K. Liu, Nature of ferroelectric-paraelectric phase transition and origin of negative thermal expansion in $PbTiO_3$, Phys. Rev. B 91 (2015) 024104, doi: 10.1103/PhysRevB.91.024104.
[27] J. Chen, X. Xing, C. Sun, P. Hu, R. Yu, X. Wang, L. Li, Zero thermal expansion in $PbTiO_3$ -based perovskites, J. Am. Chem. Soc. 130 (2008) 1144–1145, doi: 10.1021/ja7100278.
[28] P.-E. Janolin, P. Bouvier, J. Kreisel, P.A. Thomas, I.A. Kornev, L. Bellaiche, W. Crichton, M. Hanfland, B. Dkhil, High-pressure $PbTiO_3$: an investigation by Raman and X-ray scattering up to 63 GPa, Phys. Rev. Lett. 101 (2008) 237601, doi: 10.1103/PhysRevLett.101.237601.
[29] B. Im, H. Jun, K.H. Lee, S.H. Lee, I.K. Yang, Y.H. Jeong, J.S. Lee, Fabrication of a vertically aligned ferroelectric perovskite nanowire array on conducting substrate, Chem. Mater. 22 (2010) 4806–4813, doi: 10.1021/cm101412d.
[30] G. Pilania, R. Ramprasad, Complex polarization ordering in $PbTiO_3$ nanowires: a first-principles computational study, Phys. Rev. B 82 (2010) 155442, doi: 10.1103/PhysRevB.82.155442.
[31] Z.-K. Liu, Z.G. Mei, Y. Wang, S.-L. Shang, Nature of ferroelectric–paraelectric transition, Philos. Mag. Lett. 928683541 (2012) 399–407, doi: 10.1080/09500839.2012.683541.
[32] Z. Xiao, Z. Ren, Z. Liu, X. Wei, G. Xu, Y. Liu, X. Li, G. Shen, G. Han, Single-crystal nanofibers of Zr-doped new structured $PbTiO_3$: hydrothermal synthesis, characterization and phase transformation, J. Mater. Chem. 21 (2011) 3562, doi: 10.1039/c0jm04212a.
[33] H. Cheng, J. Ma, Z. Zhao, D. Qiang, Y. Li, X. Yao, Hydrothermal synthesis of acicular lead titanate fine powders, J. Am. Ceram. Soc. 75 (1992) 1123–1128, doi: 10.1111/j.1151-2916.1992.tb05548.x.
[34] M.-J. Zhou, Y. Wang, Y. Ji, Z.-K. Liu, L.-Q. Chen, C.-W. Nan, First-principles lattice dynamics and thermodynamic properties of pre-perovskite $PbTiO_3$, Acta Mater. 171 (2019) 146–153, doi: 10.1016/j.actamat.2019.04.008.
[35] O.G. Vendik, S.P. Zubko, I. Introduction, Ferroelectric phase transition and maximum dielectric permittivity of displacement type ferroelectrics, J. Appl. Phys. 88 (2000) 5343–5350.
[36] J. Wang, Switching mechanism of polarization vortex in single-crystal ferroelectric nanodots, Appl. Phys. Lett. 97 (2010) 192901, doi: 10.1063/1.3515847.
[37] Y.L. Li, S.Y. Hu, Z.K. Liu, L.Q. Chen, Effect of substrate constraint on the stability and evolution of ferroelectric domain structures in thin films, Acta Mater. 50 (2002) 395–411, doi: 10.1016/S1359-6454(01)00360-3.
[38] M.J. Haun, E. Furman, S.J. Jang, H.A. McKinstry, L.E. Cross, Thermodynamic theory of $PbTiO_3$, J. Appl. Phys. 62 (1987) 3331–3338, doi: 10.1063/1.339293.
[39] J.J. Wang, X.Q. Ma, Q. Li, J. Britson, L.Q. Chen, Phase transitions and domain structures of ferroelectric nanoparticles: Phase field model incorporating strong elastic and dielectric inhomogeneity, Acta Mater. 61 (2013) 7591–7603, doi: 10.1016/j.actamat.2013.08.055.
[40] Y.L. Li, S.Y. Hu, Z.K. Liu, L.Q. Chen, Effect of electrical boundary conditions on ferroelectric domain structures in thin films, Appl. Phys. Lett. 81 (2002) 427–429, doi: 10.1063/1.1492025.
[41] V.I. Levitas, Thermodynamically consistent phase field approach to phase transformations with interface stresses, Acta Mater 61 (2013) 4305–4319, doi: 10.1016/j.actamat.2013.03.034.
[42] V.I. Levitas, M. Javanbakht, Surface tension and energy in multivariant martensitic transformations: phase-field theory, simulations, and model of coherent interface, Phys. Rev. Lett. 105 (2010) 165701, doi: 10.1103/PhysRevLett.105.165701.
[43] A.N. Morozovska, E.A. Eliseev, M.D. Glinchuk, Ferroelectricity enhancement in confined nanorods: direct variational method, Phys. Rev. B. 73 (2006) 214106, doi: 10.1103/PhysRevB.73.214106.
[44] E.A. Eliseev, A.N. Morozovska, General approach for the description of size effects in ferroelectric nanosystems, J. Mater. Sci. 44 (2009) 5149–5160, doi: 10.1007/s10853-009-3473-0.
[45] A.K. Tagantsev, Landau expansion for ferroelectrics: which variable to use? Ferroelectrics 375 (2008) 19–27, doi: 10.1080/00150190802437746.
[46] M. Budimir, D. Damjanovic, N. Setter, Large enhancement of the piezoelectric response in perovskite crystals by electric bias field antiparallel to polarization, Appl. Phys. Lett. 85 (2004) 2890–2892, doi: 10.1063/1.1799231.
[47] R.C. Dorf, The Electrical Engineering Handbook, Second Edition, 1997.